Contents lists available at ScienceDirect

Computers & Graphics

journal homepage: www.elsevier.com/locate/cag

Exploration of Blood Flow Patterns in Cerebral Aneurysms during the Cardiac Cycle

Monique Meuschke[a,b,*], Samuel Voß[a,b], Bernhard Preim[a,b], Kai Lawonn[c]

[a] University of Magdeburg, Universitätsplatz 2, 39106 Magdeburg, Germany
[b] Research Campus STIMULATE, Universitätsplatz 2, 39106 Magdeburg, Germany
[c] University of Koblenz - Landau, Universitätsstraße 1, 56070 Koblenz, Germany

ARTICLE INFO

Article history:
Received October 8, 2018

Keywords: Flow Visualization, Clustering, Medical Visualization

ABSTRACT

This paper presents a method for clustering time-dependent blood flow data, represented by path lines, in cerebral aneurysms using a reliable similarity measure combined with a clustering technique. Such aneurysms bear the risk of rupture, whereas their treatment also carries considerable risks for the patient. Medical researchers emphasize the importance of investigating aberrant blood flow patterns for the patient-specific rupture risk assessment and treatment analysis. Therefore, occurring flow patterns are manually extracted and classified according to predefined criteria. The manual extraction is time-consuming for larger studies and affected by visual clutter, which complicates the subsequent classification of flow patterns. In contrast, our method allows an automatic and reliable clustering of intra-aneurysmal flow patterns that facilitates their classification. We introduce a similarity measure that groups spatio-temporally adjacent flow patterns. We combine our similarity measure with a commonly used clustering technique and applied it to five representative datasets. The clustering results are presented by 2D and 3D visualizations and were qualitatively compared and evaluated by four domain experts. Moreover, we qualitatively evaluated our similarity measure.

1. Introduction

For the diagnosis and treatment assessment of cardiovascular diseases (CVDs), the analysis of patient-specific morphological and hemodynamic data is necessary [1]. This work focuses on cerebral aneurysms, characterizing pathologic dilatations of intracranial arteries. Their most serious consequence is their rupture leading to a subarachnoid hemorrhage (SAH), which is associated with a high mortality and morbidity rate [2]. In case of a rupture, a treatment is essential. A frequently used treatment option is *stenting*, where the flow is diverted from the aneurysm sac by an expandable medical implant (stent). However, treatment is also associated with a considerable risk of severe complications, such as post-treatment hemorrhaging, which can exceed the natural rupture risk [3]. In most cases an aneurysm is asymptomatic and will never rupture. But due to the poor prognosis of a SAH, aneurysms are usually treated. Thus, it is highly desirable to better understand the individual rupture risk and to restrict treatment to high-risk patients.

Unfortunately, the aneurysm progression and rupture depends on different factors such as genetics, morphological conditions and hemodynamics, where their interplay is not well understood [4]. Hemodynamic data are characterized by quantitative parameters such as Wall Shear Stress (WSS), and qualitatively, e.g., w.r.t. specific flow patterns, such as vortices. Moreover, flow patterns are assumed to be related to the success of treatment and their distance to the vessel wall seems to be an important factor for the assessment of the aneurysm's state [5].

To investigate the influence of flow patterns on the aneurysm's rupture, medical studies are performed [6]. There-

*Corresponding author: Tel.: +49-391-675 2759; fax: +49-391-671 1164 ;
e-mail: meuschke@isg.cs.uni-magdeburg.de (Monique Meuschke)

fore, hemodynamic information are used that can be obtained by Computational Fluid Dynamic (CFD) simulations. Flow patterns are extracted and manually classified according to their *complexity* and *stability* during the cardiac cycle. The results were compared between ruptured and non-ruptured cases to identify characteristics associated with rupture. This is a time-consuming process in which flow patterns more distant to the wall are easily overlooked due to visual clutter and occlusion. To uncover correlations between flow patterns and the aneurysm state, more efficient analysis techniques are essential. This requires a reliable grouping of blood flow-representing path lines characterizing individual flow patterns.

In this work, we present a method for an automatic clustering of blood flow in cerebral aneurysms over the cardiac cycle. Blood flow-representing path lines were integrated in simulated CFD data and clustered to obtain groups with similar flow behavior. For this purpose, we extend an established similarity measure for streamlines to path lines that incorporates their temporal component. To explore the behavior of individual flow patterns, we provide 2D views linked to a 3D depiction of the aneurysm wall and internal blood flow. The 2D views enable an occlusion-free visualization of flow patterns, including their distance to the vessel wall. The 3D visualization represents the focus upon which the exploration of morphological aneurysm characteristics together with the blood flow information over the cardiac cycle takes place. We integrate these techniques into a framework that we developed in collaboration with domain experts. In summary, we make the following contributions:

- An automatic clustering of intra-aneurysmal flow patterns over the cardiac cycle.
- A linked 2D and 3D view of the aneurysm surface and internal flow patterns for an interactive exploration.

2. Related Work

Our work is related to partition-based blood flow visualization, as well as the visual exploration of aneurysm data.

2.1. Partition-Based Flow Visualization

Partitioning techniques decompose flow into areas of common structure to investigate hemodynamics. Graphical representatives of flow regions can be computed to generate a visual summary or a subsequent visualization can be restricted to regions with specific properties, e.g., vortices. Such techniques are mainly based on integral curves, since in contrast to local vectorial flow data, they represent continuous flow patterns. The partitioning is performed in a user-guided [7, 8, 9] or automatic fashion [10, 11, 12, 13, 14]. Less frequently, local flow vectors [15] or aneurysm wall properties [16, 17] are employed.

User-guided techniques partition integral curves based on *line predicates* (LP) [18], which are Boolean functions that decide if integral curves fulfill properties of interest. Gasteiger et al. [8] applied LP to CFD data of cerebral aneurysms to extract flow features, e.g., the *inflow jet* – the structure of high-speed, parallel aneurysm inflow and the *impingement zone* – the region where the inflow jet hits the wall with high impact. Based on this, a comparative visualization for evaluating various stent configurations was presented, integrating morphological and hemodynamic data [19]. Born et al. [7] utilized LP to identify relevant flow features such as jets and vortices in measured cardiac data. Köhler et al. [9] used different local vortex criteria as LP to filter path lines that represent aortic vortices.

Automatic techniques employ a data-driven approach and utilize clustering methods to group integral curves based on a similarity measure. McLoughlin et al. [14] introduced a streamline similarity measure by computing geometrical features based on the underlying vector field and used an agglomerative hierarchical clustering (AHC) with average link for partitioning. Their method was applied to time-dependent data by extracting the geometrical features from the vector field of the corresponding time step. However, the temporal component was not directly considered. Two geometrically similar path lines occurring in non-overlapping time intervals would have a high similarity. Oeltze et al. [13] compared multiple streamline clusterings in the context of aneurysm hemodynamics. Streamline similarities were computed based on line geometry [20]. They conducted a quantitative evaluation of k-Means, AHC, and spectral clustering (SC) w.r.t. cluster purity measures, where SC as well as AHC with average link and Ward's method performed best. Furthermore, a visual summary of blood flow was proposed, containing one representative streamline per cluster to reduce visual clutter. Englund et al. [10] employed a partitioning approach for the exploration of aortic hemodynamics. They used the Finite-time Lyapunov Exponent to measure the separation of path lines and coherent areas are derived. Liu et al. [11] measured path line similarities using an octree. The space is divided into cubes either by equidistant length or by adaptive length that depends on the features of the underlying vector field. A sequence is assigned to the path lines that incorporates the passed cubes, where the similarity is based on the longest common sequence. Meuschke et al. [12] compared multiple clustering methods of path lines representing aortic vortex flow. Path line similarities were computed based on the spatio-temporal coordinates of line endpoints and the line's average distance to the vessel centerline. AHC with average link performed best in separating vortices.

We introduce a time-dependent clustering of flow-representing path lines by extending an eligible approach for streamline clustering [20]. In contrast to the streamline similarity measure by McLoughlin et al. [14], our method directly incorporates the temporal component. If a flow pattern occurs, decays and reoccurs during the cardiac cycle, our method results in several clusters. This is required, since stability of flow patterns is an important criterion in medical studies to predict the rupture risk [6]. Existing methods are not able to represent instable flow patterns by different clusters. Moreover, compared to existing time-dependent clustering approaches [11, 12], we are not dependent on the centerline or the underlying partitioning of the space.

2.2. Visualization and Exploration of Aneurysms

To visualize the aneurysm morphology, Hastreiter et al. [21] presented a direct volume rendering (DVR) method. Tomandl et

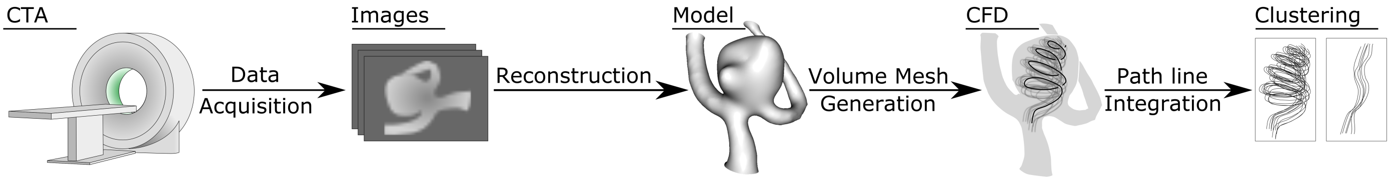

Fig. 1. The preprocessing pipeline. Based on clinical image data, the 3D vessel surface is reconstructed. From this, a volume mesh is generated as input for the CFD simulation. Based on the simulated data, flow-representing path lines are integrated, which are finally clustered to analyze flow patterns.

al. [22] introduced a standardized vessel depiction using DVR for a more objective assessment of the aneurysm morphology.

Several works parametrize the aneurysm surface to generate more abstract representations. Goubergrits et al. [23] mapped the aneurysm to a uniform sphere to analyze statistical WSS distributions. Meuschke et al. [24] generated a 2D aneurysm map by using *least squares conformal maps* [25] that provides an occlusion-free overview visualization. Tao et al. [26] presented the *VesselMap*, a 2D mapping of an aneurysm and parent vasculature formulated as a graph layout optimization problem.

For the simultaneous exploration of anatomical and vectorial flow data, Gasteiger et al. [27] introduced the *FlowLens*, an interactive focus-and-context approach. However, outside the lens area, the flow cannot be observed. To improve this, Lawonn et al. [28] provided a vessel visualization such that the morphology can be better perceived and the flow is always visible. For a more detailed analysis, Neugebauer et al. [17] developed a qualitative exploration of near-wall hemodynamics in cerebral aneurysms. Several 2D widgets are used to simplify streamlines at different surface positions. Gambaruto et al. [29] analyzed flow features that are potentially related to aneurysm rupture. They extracted critical points related to WSS, vortices and surface shear lines, which are visualized using standard techniques such as glyphs, vortex-isosurfaces, and streamlines. Lawonn et al. [30] presented a framework for an occlusion-free blood flow visualization by using illustrative techniques. Meuschke et al. [24] extended this approach to investigate morphological and hemodynamic data simultaneously by providing a low-occlusion 2.5D view linked to a 3D aneurysm depiction.

We visualize flow patterns using a 2D map linked to a 3D aneurysm depiction. Existing methods need a lot of user interaction, i.e., interactive lenses [27] or manually selected seeding regions [17] to find suspicious flow patterns. Based on our clustering, our visualizations allow a detailed exploration of individual flow patterns and an assessment of the most prominent flows without a manual search. In contrast to existing map-based visualizations that enable an exploration of scalar data, our aneurysm map provides also the depiction of vectorial flow data. With this, possible correlations between mechanical wall properties and blood flow characteristics can be explored.

3. Medical and Hemodynamic Background

In clinical practice, several morphological features of aneurysms, such as size, shape and location, are used to assess the rupture risk [31]. These parameters differ statistically significant between ruptured and non-ruptured cases [4, 23]. However, the patient-specific rupture risk cannot be reliably estimated using these features. The internal blood flow seems also to play an important role in the initiation, progression, and aneurysm rupture [4]. CFD allows modeling of the hemodynamics resulting in quantitative and qualitative flow parameters [32]. Quantitative parameters are, e.g., WSS, whereas qualitative features comprise specific flow patterns such as vortices.

To investigate how flow patterns influence rupture, medical studies manually evaluate the complexity and temporal stability of flow patterns in ruptured and non-ruptured cases [6, 33, 34, 35]. Cebral et al. [6] distinguished three flow types: flow with an unchanging direction, flow with a changing direction and vortical flow. They also considered the size of the impingement region and the inflow jet. Non-ruptured aneurysms showed mainly type one with some vortical flow, large impingement regions, and large jets. In contrast, type two with vortical flow was mainly seen in ruptured aneurysms together with small impingement regions and small jets. Castro et al. [34] correlated rupture to inflow jet structure and peak WSS. Nakayama et al. [35] classified systolic flow in cerebral aneurysms dependent on their rotational position. They distinguished the side-type pattern, where the flow began from the side of the ostium, separating the aneurysm from the parent vessel, and the split type, where the flow began from the ostium center. Recently, Futami et al. [33] classified cerebral aneurysms into four types based on the relationship between morphology and inflow jet. Neck-limited jets were correlated to rupture.

4. Data Acquisition and Preprocessing

For the CFD simulation, a polygonal model of the vascular wall is extracted from clinical CT angiographic images using the pipeline by Mönch et al. [36], see Figure 1. A threshold-based segmentation, followed by a connected component analysis with a subsequent isosurface extraction (Marching Cubes) is applied. Occurring segmentation errors were manually corrected and the mesh quality was optimized [37]. Based on the optimized mesh, a hybrid volume mesh was generated as input for the simulation. CFD numerically calculates the patient-specific hemodynamics by solving the Navier-Stokes equations, where blood is considered as an incompressible Newtonian fluid [38]. The inlet boundary conditions are derived from two patient-specific velocity profiles [38], lasting 0.93 s and 0.81 s respectively, depending on the patient's heart rate during acquisition. These profiles are used for the remaining cases due to the absence of similar data. This is a reasonable step, since any applied patients heart rate is only a snapshot and varies due to physical activity and health condition. A rigid vessel wall

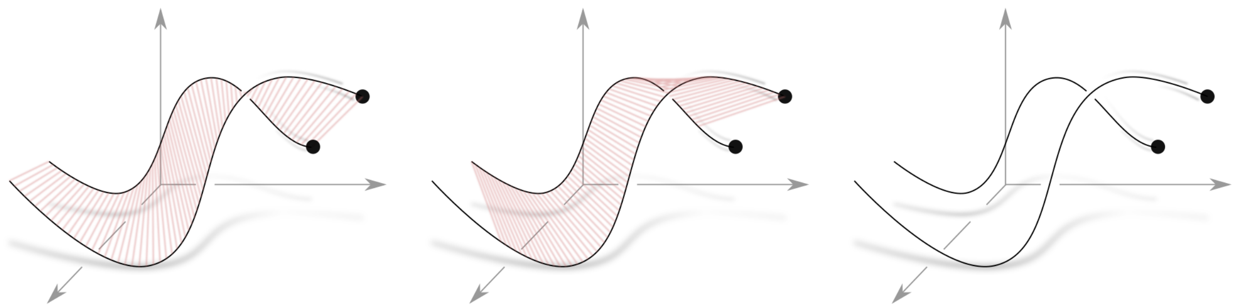

Fig. 2. Our approach computes the mean distance of two path lines at positions where the time coincides. In case 1 (left), the time interval coincides, in case 2 (middle), parts of the path lines share the same time interval, and in case 3 (right) the path lines occur at different points in time.

was assumed and the outlet pressure was defined as zero, since only the relative pressure is calculated. For every dataset, two cardiac cycles were simulated, where the first was discarded to avoid inaccuracies from initialization. Based on the CFD results, path lines are integrated with an adaptive fifth order Runge-Kutta method every 0.01 s on the ostium, to assess the aneurysm inflow. For seeding, the centers of the ostium triangles are used resulting in a homogeneously distributed number of vertices to avoid under- and over-representation of flow parts. The integration terminates if the current path line leaves the spatio-temporal domain. Finally, the ostium surface was used to remove path line parts outside the aneurysm that are not relevant for the clustering process.

5. Requirement Analysis

Our approach is based on the discussion with three domain experts: one neuroradiologist treating and researching cerebral aneurysms and two engineers working on CFD simulations for cerebral aneurysms. We asked them about the importance of analyzing flow patterns over the cardiac cycle that was rated as highly important by all experts (details can be found in Sec. 8.4). The most relevant scientific task of the neuroradiologist is to assess the rupture risk. Similar to other medical studies [6, 33, 34, 35], morphological and hemodynamic features are therefore explored, which might lead to a patient-specific assessment of the rupture risk in the future. This includes a comparison of ruptured and non-ruptured datasets. Based on this, neuroradiologists have to make optimal treatment decisions. Therefore, they analyze how flow patterns and scalar flow parameters are changing depending on different stent configurations. In contrast, an important task for CFD engineers is to validate their simulation results according to physical plausibility. In addition, a standardized classification method enables an objective comparison of datasets w.r.t. the dominant flow patterns. Furthermore, the visualization of more than one physical quantity at once can help to find spots of fluid wall interactions. This also requires an exploration of scalar and vectorial flow features as well as morphological properties.

The typical workflow to analyze aneurysm data is quite similar for both types of experts w.r.t. the tasks. They examine color-coded scalar parameters on the vessel surface, e.g., WSS in combination with flow-representing path lines over the cardiac cycle. For a more detailed analysis, flow patterns are manually classified by our domain experts according to the flow types defined by Cebral et al. [6]. This process is affected by visual clutter due to the flow complexity, which makes the classification error-prone. To facilitate classification of flow patterns, a computer-based detection is needed. This requires a reliable path line clustering that does not need a priori selection of the (unknown) cluster number. Therefore, a similarity measure is needed that is able to group spatio-temporally adjacent patterns. However, due to the large anatomic diversity, the automatically calculated results will not always be appropriate. Thus, the experts should be able to manually correct the results.

In order to verify and interpret the clustering results, both types of experts wanted an adequate visualization of flow patterns. A more abstract depiction of the complex flow and vessel morphology would help the neuroradiologist comparing ruptured and non-ruptured cases. According to the CFD experts, a more simplified depiction would support the assessment of the most prominent flow patterns. Moreover, the neuroradiologist want to evaluate whether local changes of flow parameters occur on morphologically abnormal wall sections to uncover possible rupture-prone correlations. Based on these discussions, we summarize the main requirements for our tool as follows:

Req. 1. Clustering. The clustering should separate spatio-temporal flow patterns without a predefined cluster number.

Req. 2. Contribution of expert knowledge. The experts should be able to correct the automatically calculated clustering results.

Req. 3. Cluster visualization. More abstract visualizations are needed that allow a simultaneous analysis of scalar and vectorial flow properties as well as a assessment of flow patterns.

6. Blood Flow Clustering

In the following, we give a detailed explanation of our path line similarity measure. We proceed with a description of the used clustering method that does not need a priori selection of the cluster number (*Req. 1*). In the remainder of this paper, we use the following notation. A path line pl consists of vertices $V = \{1, \dots, n\}$, edges $E = \{(i, i+1) \,|\, i \in \{1, \dots, n-1\}\}$, and a time set $T = \{t_1, \dots, t_n \,|\, t_i < t_{i+1}\} \in \mathbb{R}^n$. The corresponding 3D coordinates of the vertices are denoted with $\mathbf{p}_i \in \mathbb{R}^3$, $i \in V$. We use $pl(t_i) = \mathbf{p}_i$ with $i \in V$, $t_i \in T$ to denote the 3D coordinates of the path line points as a function of time.

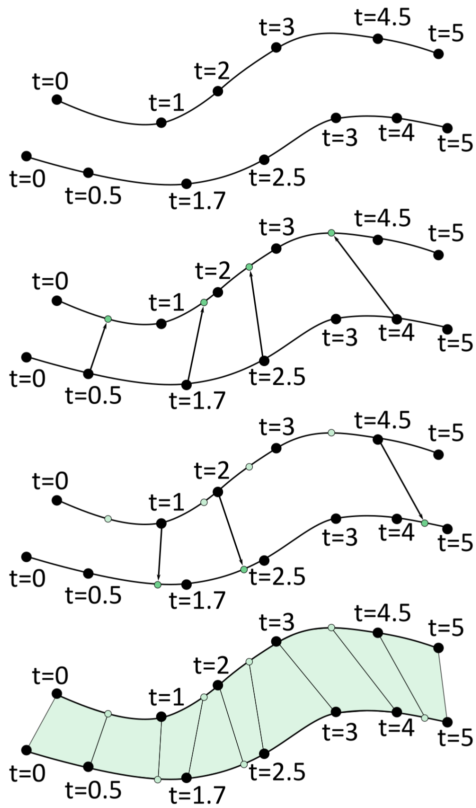

Fig. 3. To measure the mean distance of two path lines, the points of the first line with different times are projected on the other line and vice versa. Then, the mean distances of the rectangular segments are determined.

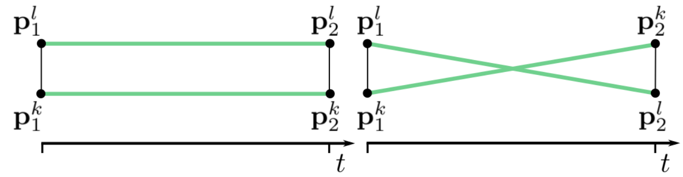

Fig. 4. Calculation of the mean distance for two path line pairs, where each line has two points. A sample-based calculation of the mean distance would result in the same distance for both pairs, although they show a different behavior. Using the integral-based calculation, the left pair has a higher mean distance than the right pair.

6.1. Calculation of the Similarity Matrix

Our path line clustering builds up on the mean of closest point distances (MCPD) [20] measure that was successfully used for streamline clustering [13]:

$$
\begin{aligned}
d_M(s_i, s_j) &= \operatorname{mean}(d_m(s_i, s_j), d_m(s_j, s_i)) \; with \\
d_m(s_i, s_j) &= \underset{p_l \in s_i,\; p_k \in s_j}{\operatorname{mean}\,\min} \|p_k - p_l\|.
\end{aligned} \tag{1}
$$

This measure determines for every point on the streamline the minimum distance to another streamline and averages it. However, it does not encode the temporal component. Our distance measure integrates the time component of path lines. Inspired by MCPD, we incorporate the mean distances of path lines.

Note, that a path line usually does not exist during the whole cardiac cycle due to the high velocities (up to 1.51 m/s) and the small spatial domain size (5-11 mm in the x,y,z-direction) [32, 38]. This further means, that the temporal components of two path lines would not have been synchronized for integration with a uniform temporal step length instead of the used adaptive step length (see Sec. 4). Thus, we have to determine corresponding path line points depending on their temporal component, which is explained in the following.

Given are two path lines pl_k, pl_l with time components $t_1^k, \ldots, t_n^k$ and $t_1^l, \ldots, t_m^l$ for which we like to calculate the mean distances. For this, we distinguish three cases, see also Figure 2:

1. $[t_1^k, t_n^k] = [t_1^l, t_m^l]$ means both path lines occur in the same time interval, see Figure 2 (left).
2. $[t_1^k, t_n^k] \neq [t_1^l, t_m^l]$ and $[t_1^k, t_n^k] \cap [t_1^l, t_m^l] \neq \emptyset$ means the path lines share a time interval, see Figure 2 (middle).
3. $[t_1^k, t_n^k] \cap [t_1^l, t_m^l] = \emptyset$ means the path lines occur in different time intervals, see Figure 2 (right).

Case 1: In this case, the time components of both path lines coincide: $[t_1^k, t_n^k] = [t_1^l, t_m^l]$. To determine the mean distance, we need points on both path lines such that their timings coincide. In general, the time components of the points on the first path line vary compared to the points on the second line, see Figure 3 (top). Therefore, we place new points on both lines such that the time components coincide, see Figure 3 (bottom). For this, we linearize the time along an edge and determine the position such that the time at this position correspond to the desired time component. This yields two path lines with the same number of points $\mathbf{p}_1^k, \ldots, \mathbf{p}_M^k$, $\mathbf{p}_1^l, \ldots, \mathbf{p}_M^l$ and the same time components $t_1^k, \ldots, t_M^k, t_1^l, \ldots, t_M^l$. Note, that $t_1^k = t_1^l, t_2^k = t_2^l, \ldots, t_M^k = t_M^l$ holds by construction of the points, thus we will omit the superscript.

Finally, we compute the $M-1$ mean distances between the path line parts given by the curves:

$$
\begin{aligned}
c_k(t) &= \mathbf{p}_i^k + t(\mathbf{p}_{i+1}^k - \mathbf{p}_i^k), \\
c_l(t) &= \mathbf{p}_i^l + t(\mathbf{p}_{i+1}^l - \mathbf{p}_i^l), \\
& \quad t \in [0,1], \;\; i \in \{1, \ldots, M-1\}.
\end{aligned} \tag{2}
$$

The mean distance of two path lines in the time interval $[t_i, t_{i+1}]$ could be determined by a sample-based calculation. However, the resulting mean distance would be dependent on the number of samples, see Figure 4. Here, both pairs would have the same mean distance, although their behavior is different. Generating enough samples would converge to the correct mean distance, but would increases the calculation effort. To avoid such inaccuracies, the mean distance of both path lines in the time interval $[t_i, t_{i+1}]$ is determined by:

$$
\overline{D}^{kl}(t_i, t_{i+1}) = \int_0^1 d(t)\,\mathrm{d}t,
$$

with $d(t) = \|c_k(t) - c_l(t)\|$. Thus, the mean distance of two moving particles is determined by a novel approach using the integral of the distances, which is of the form:

$$
\overline{D}^{kl}(t_i, t_{i+1}) = \int_0^1 d(t)\,\mathrm{d}t = \int_0^1 \sqrt{a + 2bt + ct^2}\,\mathrm{d}t, \tag{3}
$$

see Section 11 for details.

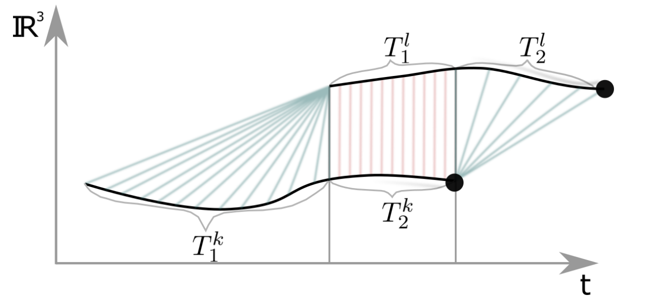

Fig. 5. Calculation of path line distances for Case 2. Therefore, (at most) three sets, T_1^k, T_2^k and T_2^l, are distinguished, whereas $T_2^k = T_1^l$.

Therefore, we determined the $M-1$ mean distances between the path line parts $\overline{D}^{kl}(t_1,t_2), \overline{D}^{kl}(t_2,t_3), \ldots, \overline{D}^{kl}(t_{M-1},t_M)$, which yields the overall mean distance:

$$\overline{D}_{kl} = \frac{1}{t_M - t_1} \sum_{i=1}^{M-1} (t_{i+1} - t_i) \cdot \overline{D}^{kl}(t_i, t_{i+1}). \tag{4}$$

Case 2: For case 2, we determine the distance of the overlapping temporal part with Eq. 4. Thus, there exist two disjoint sets that partitioned the time set of the path lines such that $T_1^k \cup T_2^k = [t_1^k, t_n^k]$ and $T_1^l \cup T_2^l = [t_1^l, t_n^l]$. Without loss of generality, we assume $T_2^k = T_1^l$, see Figure 5. Then, the distance of the set T_2^k is determined based on Eq. 4. To consider the missing parts T_1^k and T_2^l, we calculate the mean distance with Eq. 4, but change the curves given in Eq. 2. For T_1^k, we alter c_l to $c_l = pl_l(t_1^l) = \mathbf{p}_1^l$ (and for T_1^k, we set $c_k = \mathbf{p}_n^k$).
Case 3: In case 3, the time intervals do not overlap. Without loss of generality, we assume $t_n^k < t_1^l$. Again, we determine the mean distance with Eq. 4, but change the curves given in Eq. 2. First, we set $c_k = \mathbf{p}_n^k$ and determine $\overline{D}^{kl}$ (to all line segments on pl_l). Then, we set $c_l = \mathbf{p}_1^l$, determine $\overline{D}^{kl}$ (to all line segments on pl_k), and add this to the result.
Jaccard Matrix: So far, we determined the mean distances of two path lines as basis for the similarity calculation. Besides this, we want to ensure that two path lines of case 1 are more similar than path lines of case 3. For this, we compute a Jaccard matrix J, which uses a Jaccard metric. For two path lines pl_k, pl_l with time components $T_k = \{t_1^k, \ldots, t_n^k\}$ and $T_l = \{t_1^l, \ldots, t_m^l\}$, the Jaccard matrix is given by $(J)_{kl} = 1 - \frac{\max(T_k \cap T_l) - \min(T_k \cap T_l)}{\max(T_k \cup T_l) - \min(T_k \cup T_l)}$. In case $T_k \cap T_l = \emptyset$, we set $\max(T_k \cap T_l) = \min(T_k \cap T_l) = 0$. Thus, if $(J)_{kl} = 0$, both path lines exist in the same time interval (case 1). If $(J)_{kl} = 1$, both lines occur at different points in time (case 3). Otherwise, they share a time interval (case 2).
Distance Matrix: Based on the cases 1, 2, and 3 we construct the distance matrix $\mathbf{D}$ with $(D)_{ij} = \overline{D}_{ij} + J_{ij} \cdot \max_{ij} \overline{D}_{ij}$. Note, with the construction of the Jaccard matrix, we ensure that $D(case\,1) \leq D(case\,3)$. For case 2, we have to split the distance calculation into (at most) three parts, one or two parts of time intervals that do not overlap. In case 3, we have two components, which are used to determine the similarity.

6.2. Path Line Clustering

The distance matrix is used as input for the path line clustering. Each path line is assigned to exactly one cluster. Oeltze et al. [13] recommend to use AHC or SC to group streamlines in cerebral aneurysms. We extend their similarity measure for applying it on path lines and used AHC. Density-based approaches such as DBSCAN are also used to cluster integral lines [10, 12]. However, we reject DBSCAN, since two thresholds have to be defined, which essentially determine the cluster structure and an appropriate threshold selection can be tedious [12]. Moreover, using AHC allows to compare our similarity measure to existing techniques [12, 13] that used AHC to cluster blood flow-representing lines.

AHC is a bottom-up approach, which builds a hierarchical decomposition of a set consisting of n objects based on the similarity matrix. At the beginning, each object is initialized as a cluster. In an iterative process, the two most similar clusters are fused based on $\mathbf{D}$ and a measure of cluster proximity until a single cluster remains. We used average link that is defined as the average distance of all object pairs from two clusters. The cluster hierarchy enables a fast analysis of different cluster numbers. Furthermore, AHC is non-parametric, except for $\mathbf{D}$ and the proximity measure. To reduce the effort for selecting an appropriate cluster number, we aim to make a "good guess" using the *L-method* [39]. If the automatically calculated number is not appropriate, the expert can incorporate his expert knowledge by chaining the cluster number (*Req. 2*).

7. Visualization of Blood Flow Clusters

The path line clusters are visualized in two juxtaposed render contexts that are linked to each other. The first one shows the clusters within the 3D aneurysm, whereas the second provides a more abstract depiction. Here, the clusters are visualized as 2D structures. In the following, we comment on the design decisions for the different views and their interplay.

7.1. 3D Cluster Visualization

The 3D aneurysm view enables a detailed exploration of possible correlations between individual flow patterns that are associated with an increased risk of rupture and high-risk wall regions. Therefore, the aneurysm surface is depicted following the approach by Meuschke et al. [24]. This enables a simultaneous exploration of two user-selected scalar fields, see Figure 6 (left). The first is depicted using a gray-to-red color scale and the second one is visualized using an image-based hatching scheme. The blood flow is represented by lines and color-coded according to a user-selected property, e.g., the velocity. To analyze scalar data and the internal flow simultaneously, we applied *Fresnel shading* to the vessel's transparency as suggested by Gasteiger et al. [40], see Figure 6 (right).

The simultaneous depiction of all path lines would lead to visual clutter. Therefore, we determined a representative for each cluster that summarizes the blood flow and enables the perception of inner flow structures. We used *density-based representatives* [41] to approximate the shape of the clusters. The method is based on generating a Cartesian grid around the cluster using its axis-aligned bounding box. The grid resolution corresponds to the resolution of the image data that was used to reconstruct the aneurysm morphology. For each voxel of the grid, a density

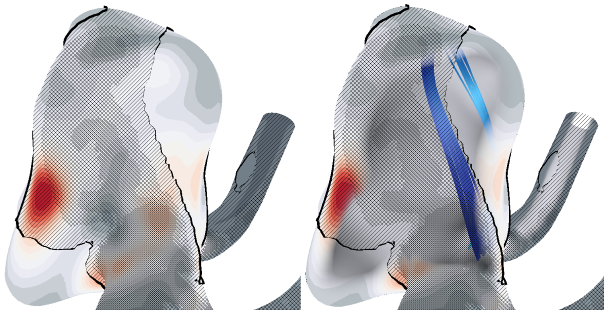

Fig. 6. Simultaneous exploration of two scalar fields on the aneurysm surface using color-coding (here WSS is depicted) and an image-based hatching scheme (here pressure is depicted)(left). To reveal the qualitative flow behavior Fresnel shading is applied to the surface (right).

value is determined by counting the number of passing lines. Finally, the densities per line are integrated and the line with the highest value is used as representative. The representatives are shaded as tubes to improve their perception from a more distant point of view. The user can select a specific representative by clicking into the scene, which activates the rendering of the corresponding path lines of that cluster. This allows a targeted exploration of suspicious flow patterns.

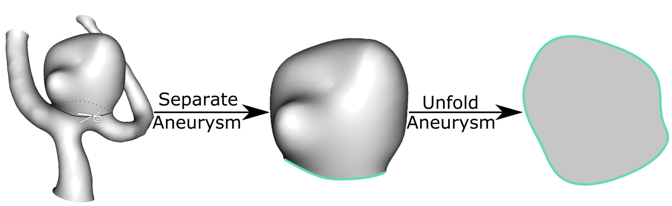

Fig. 7. For generating the 2D map, the user defines markers along the ostium that are connected to a cut line. The aneurysm surface is unfolded where the ostium is emphasized in the map.

7.2. 2D Cluster Visualization

In some cases, the aneurysm morphology is very complex. A very irregularly deformed surface complicates the simultaneous exploration of internal flow patterns and scalar wall properties. Manual rotations of the surface are necessary to perceive the flow behavior and to detect critical wall regions. The time-dependent behavior of the data further complicates the exploration, because it is almost impossible to find critical regions during animation, since the rotation process itself needs a certain amount of time. To facilitate the flow pattern analysis, we provide more abstract visualizations where the aneurysm surface and the clusters are depicted as 2D structures in two ways.

7.2.1. Map-Based Cluster Visualization

Similar to Meuschke et al. [24], we provide a 2D aneurysm map in an additional view to avoid visual clutter. The map ensures an occlusion-free exploration of a chosen scalar quantity and shows the flow behavior of individual clusters. Therefore, the path line points of a user-selected cluster are projected onto the map and are visualized as circles by applying depth-dependent halos [42]. In the following, we describe the map generation, including the projection and visualization of the path lines.

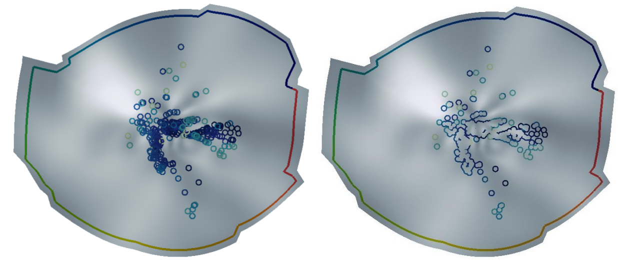

Fig. 8. Mapping of the path lines from 3D to the 2D aneurysm map. The path line points are rendered as circles, which leads to occlusion problems (left). To avoid this, we applied depth-dependent halos to them (right).

Aneurysm Separation. The generation of the map requires a separation of the aneurysm surface from the parent vessel geometry, see Figure 7. For this, we asked the user to delineate the ostium, which is achieved by generating a curve around the aneurysm. The user clicks on the surface, which yields consecutive points on the surface mesh. Once the user finished the drawing, these points are connected to a closed curve by applying the *Dijkstra* algorithm that determines the shortest path based on the Euclidean distances. Then, the surface is cut along this curve to separate the aneurysm part, which is indicated by two other user-selected points on the aneurysm region.

Aneurysm Mapping. After separation, the aneurysm part is used to calculate the map. The map is determined by a parametrization algorithm that maps every point $\mathbf{p}_i \in \mathbb{R}^3$ on the surface mesh to a point $\mathbf{p}'_i \in \mathbb{R}^2$ in the plane. Similar to Meuschke et al. [24], we employ *least squares conformal maps* (LSCM) to obtain a 2D aneurysm map [25]. LSCM employs the conformality condition, which states that the gradients of the 2D coordinates are perpendicular $\nabla v = (\nabla u)^\perp$, where $\perp$ denotes the counterclockwise rotation of $90°$ around the normal $\mathbf{n}$. This method is boundary-free and only two points need to be set as constraints for the parametrization. To establish a spatial correlation between the 2D map and the 3D view, the cut line is color-coded in both views, see Figure 8. Moreover, the user can pick a specific point on the map and the camera rotates automatically to the corresponding 3D position in a smooth way.

Path Line Mapping. After generating the 2D map, the path lines are projected on the map. Thus, for each path line point $\mathbf{p}_i$ the nearest surface point of the aneurysm part $\mathbf{p}_j$ is determined based on the Euclidean distance, see Figure 9a. For this, $\mathbf{p}_i$ is orthogonally projected into the triangle's plane defined by its normal. After projection, we check if the projected point lies inside the triangle by computing the barycentric coordinates. If the point lies inside the triangle, we determine the distance of $\mathbf{p}_i$ and the projection and store the previously determined barycentric coordinates of the triangle. In case the projected point lies not inside the triangle, we compute the nearest point on the triangle's boundary. For this, the distance of $\mathbf{p}_i$ and the three edges is determined. Again, we store the minimum distance and the barycentric coordinates of the closest point with the triangle.

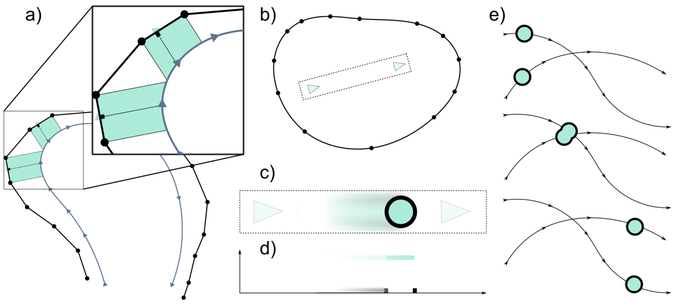

Fig. 9. First, the path line points are projected onto the aneurysm surface a). The projected points are used for the 2D map where a quad is generated around consecutive path line points b). For every point in time a circle is generated between the projected points c). The contour of the circle is transformed behind the circle itself d). This yields non-overlapping contours during the animation e).

This procedure is repeated with all triangles on the aneurysm part such that we obtain the minimum distance, the barycentric coordinates of the closest point, and the associated triangle.

Then, all path line points $\mathbf{p}_i$ are projected on the 2D map yielding $\mathbf{p}'_i$. To ensure a smooth animation of the points, we generate quads on the GPU for the successive path line points $\mathbf{p}'_i$ and $\mathbf{p}'_{i+1}$, see Figure 9b. The quads are equipped with a coordinate system that reflects the extent of the quad. In $y-$direction we have $[-\sqrt{r}, \sqrt{r}]$ and in $x-$direction we have $[-\sqrt{r}, \|\mathbf{p}_{i+1} - \mathbf{p}_i\| + \sqrt{r}]$. Here r is used for the radius of the drawn circle that represents the animated path line point. A circle is drawn on the quad if the animation time t is in $[t_i, t_{i+1}]$ (the time interval of the current time period), see Figure 9c. Then, we define $X(t) = \frac{t-t_i}{t_{i+1}-t_i} \cdot \|\mathbf{p}_{i+1} - \mathbf{p}_i\|$ and draw a white filled circle if $(x - X(t))^2 + y^2 \leq r^2$, again x, y are the coordinates of the quad, see Figure 9d. In case that $(x - X(t))^2 + y^2 \geq r^2$ and $(x - X(t))^2 + y^2 \leq (r + c)^2$ holds, where c denotes the thickness of the contour, we use a colored outline and set the depth of these fragments higher than the (white filled) circle, see Figure 10. This avoids overdraw between overlapping circles, see Figure 9e. However, the user can switch between the depth-dependent halos and the more cluttered image, see Figure 8. The circle contours can be color-coded according to a user-selected scalar field, e.g., the distance of the flow to the aneurysm wall, using a blue-to-yellow color map. Applying the depth-dependent halos avoids also occlusions between the circles and the color-coded scalar field on the 2D map, see Figure 8 (right). This enables a simultaneous exploration of scalar flow and wall properties to detect probably rupture-prone wall regions (*Req. 3*).

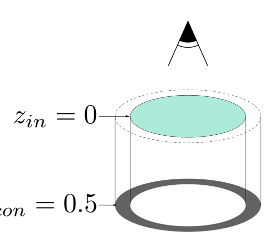

Fig. 10. Applying depth-dependent halos to the circles representing the mapped path lines. Pixels of the circle contour (z_{con}) get a higher depth value than pixels of the inner area of the circle (z_{in}).

7.2.2. *Plane-Based Cluster Visualization*

To further facilitate the perception of flow patterns, a second 2D visualization is provided. This shows the contour of the vessel surface and path lines of a user-selected cluster projected on a plane, see Figure 11. Hand-drawn sketches of aneurysms by medical experts show the aneurysm sac as most important feature pointing upwards. To fulfill this, the aneurysm has to be oriented along the y-axis of the underlying coordinate system, see Figure 11 (right). Moreover, an appropriate view should show the maximum extent of a cluster. To construct a projection plane that fulfills both conditions, we perform a principal component analysis (PCA) of the ostium positions and determine the eigenvectors $\mathbf{e}_{oi}$ with $i \in 1,2,3$. By using the ostium positions instead of all aneurysm vertices, the viewpoint selection is more independent from the aneurysm shape. We take the eigenvector of the ostium $\mathbf{e}_{o3}$ with the smallest magnitude, which runs similar to the y-axis. Moreover, we perform a PCA of the spatial path line point positions of the cluster and determine the corresponding eigenvectors $\mathbf{e}_{ci}$ with $i \in 1,2,3$. Afterwards, we calculate the scalar product between the $\mathbf{e}_{ci}$ and $\mathbf{e}_{o3}$. The eigenvector, which is most parallel to $\mathbf{e}_{o3}$ is used as first plane vector. If this vector runs in the opposite direction of $\mathbf{e}_{o3}$, we invert its direction. From the remaining two $\mathbf{e}_{ci}$, we choose the one with the largest eigenvalue as second plane vector. If the eigenvalues of both vectors are the same, we take the first one. The remaining $\mathbf{e}_{ci}$ defines the view direction of the virtual camera. Finally, we project $\mathbf{e}_{o3}$ into the constructed plane and rotate the plane that $\mathbf{e}_{o3}$ runs along the y-axis. This guarantees a view, where the aneurysm points upwards. To calculate the surface contour, we used the approach by Lawonn et al. [28]. The contour results from the positions at which the surface normal and the view direction are mutually orthogonal.

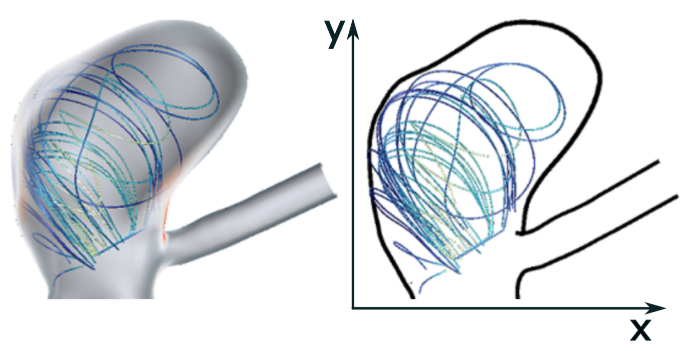

Fig. 11. Plane-based visualization of a cluster (right) from the 3D view (left). On the path lines the distance to the aneurysm surface is color-coded using a blue-to-yellow color scale.

8. Evaluation

To assess the quality of our similarity measure, we compared it with other similarity measures. Moreover, we conducted a qualitative evaluation, where participants ranked different path lines according to their similarity. We compared the rankings to our calculated similarities to assess the suitability of our method. Furthermore, we questioned experts to assess the suitability of the visualizations and their bidirectional connection.

8.1. Comparison with other Similarity Measures

We compared our similarity measure with MPCD [20], which is used to calculate streamline similarities and the approaches by Liu et al. [11] and Meuschke et al. [12] to calculate similarities between path lines. Moreover, we extended the MCPD measure by the temporal component ([20]+t). Therefore, we calculate two distance fields $d1$ and $d2$, where $d1$ represents the MCPD measure based on the 3D spatial components (x, y, z) of a path line point, and $d2$ represents the MCPD measure based on the points' temporal component t. To be independent from spatial/temporal units of the underlying domain, $d1$ and $d2$ are normalized to the range $[0, 1]$, resulting in $d1'$ and $d2'$. The final distance value between two path lines is computed by adding their corresponding $d1'$ and $d2'$ value. With this, we evaluated if such a simple integration of the temporal component leads to plausible results.

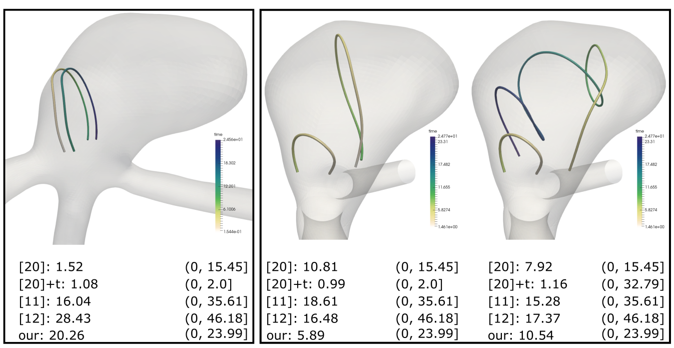

Fig. 12. Comparison of our similarity measure to MCPD [20] and existing path line similarity measures by Liu et al. [11] and Meuschke et al. [12]. Moreover, we extended MCPD by the temporal component [20]+*t*. We calculated the distance values for three path line pairs with the corresponding distance ranges in brackets. The first pair is spatially similar, but the path lines occur in different time intervals and should, therefore, not be in the same cluster (left). The second image shows two cases. The left case should be more similar than the right one due to the temporal behavior.

Figure 12 shows three pairs of path lines, where the temporal component is color-coded. Below, the corresponding distance values and ranges are listed. The higher the distance value, the less similar the lines are. The path lines in the left image are geometrically quite similar, but do not occur in the same time interval. Therefore, they should receive a high distance value. However, using MCPD the path lines have a low distance measure, since only geometrical properties are considered. With our approach, the highest distance value can be reached, ensuring that these path lines would be grouped into the same cluster only for a very low and inappropriate cluster number using AHC. For the remaining three approaches, the distance values are quite similar because of the stronger influence of geometrical properties compared to the temporal distances. The right image shows two pairs of path lines that are geometrically less similar to each other. Considering the temporal component, the left case should be more similar than the right case, which could be reached with our method. In contrast, MCPD results in a lower distance value for the right case. Integrating the temporal component for MCPD ([20]+t) results also into a lower distance for the left case. However, the distance value for the left case is quite similar to the first case in the left picture, which is not desired due to their different temporal behavior. Based on [12], the distance values are quite similar for both cases, since only the lines' start- and endpoints are considered for calculation. The distance of the right case using the method by [11] is also lower than for the left case, which shows the dependence of the underlying spatial partition into cubes. In contrast to the left pair, the right one shared some cubes.

To further evaluate our similarity measure, we compared our clusters with the results of existing similarity measures, see Figure 13. The first row shows a cluster that enters and leaves the aneurysm more distant to the wall, where the temporal component is color-coded on the lines. Using MCPD (Fig. 13a), lines with different temporal behavior are clustered together. Integrating the temporal component (Fig. 13b) leads to a cluster were path lines with a laminar and vortical behavior are grouped together. A similar result is generated with the method by [12] (Fig. 13d), since the geometrical behavior of path line points, which are no start- or endpoints is less considered. Our method (Fig. 13e) leads to a cluster that exhibits only laminar behavior without integrating path lines that occur at different times. A similar result could be generated with the method by [11] (Fig. 13c). However, this cluster contains path lines with different spatial behavior and the results were sensitive to the used cube size. Small changes of the cube size led to quite different results. The second row shows a vortical flow pattern that becomes more and more tight over the cardiac cycle. Our method (Fig. 13e) results in a cluster that shows a tight vortex at the end of the cycle. Using the other similarity measures, it is not possible to depict the decay of the vortex by individual clusters. Path lines, occurring more early in time occlude the inner vortex structure. However, to cluster instable flow patterns is important, since such patterns are correlated with rupture [6].

In addition, we artificially generated a vortex using:

$$C_i(u) = \begin{pmatrix} r_i \cdot sin(u) \\ r_i \cdot cos(u) \\ u \\ (i-1)+u \end{pmatrix}, \quad i \in \{1, ..., 100\}\ ,\ u \in [0, 10\pi], \quad (5)$$

where $r_i = \frac{1}{2} cos(\frac{2\pi i}{100}) \cdot (1 + \mathrm{sgn}(cos(\frac{2\pi i}{100})))$ and

$$sgn(x) = \begin{cases} 1 & \text{if } x \geq 0 \\ -1 & \text{if } x < 0. \end{cases} \quad (6)$$

The vortex occurs, decays to a line and reoccurs over time, see Figure 14a. Due to its time-dependent behavior, five clusters are expected showing the vortex occurring and reoccurring, the transition to laminar flow, and vise versa, as well as the laminar flow itself. MCPD (Fig. 14b) and MCPD with time (Fig. 14c) are not able to separate these stages. Similar problems would arise with the method by McLoughlin et al. [14], since just geometrical features are considered for calculation, which are quite similar for the phases. The approach by Liu et al. [11] was again sensitive to the cube size and was not able to separate the laminar flow (Fig. 14d). Our method (Fig. 14f) and the measure by [12] (Fig. 14e), where the laminar stage was used as centerline, are able to distinguish the individual stages. However, for patterns that are not so perfectly symmetric such as the example in Figure 13 (DS4), the measure by [12] is not appropriate to

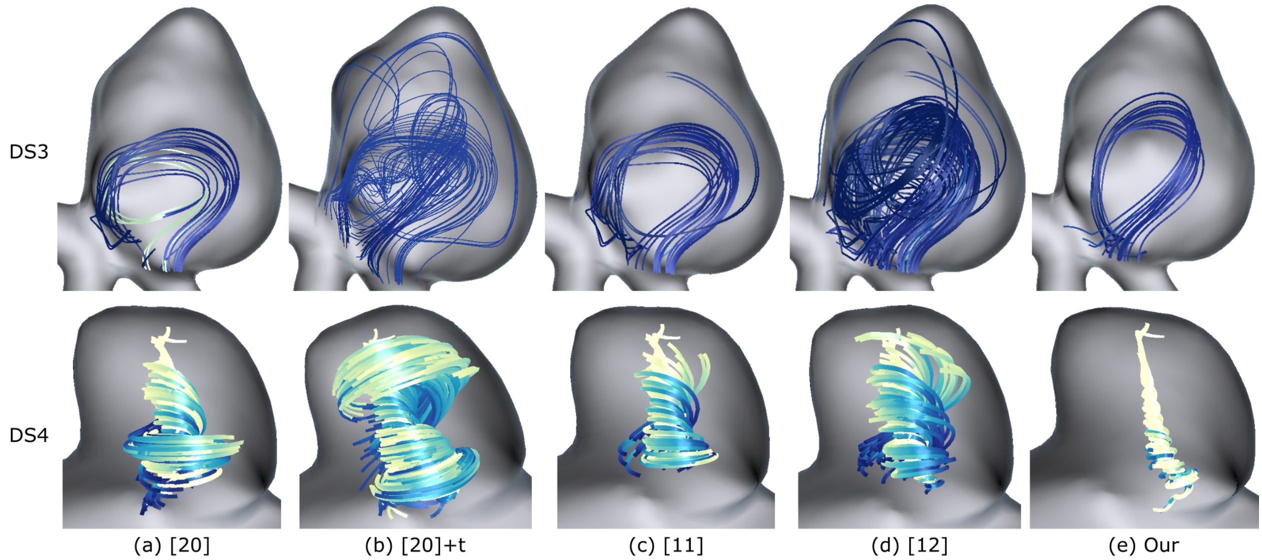

Fig. 13. Two exemplary clusters for two datasets generated with MCPD [20], MCPD [20] with time integration, the approach by Liu et al. [11] and Meuschke et al. [12] and with our method. The temporal component is color-coded using a blue-to-yellow color map.

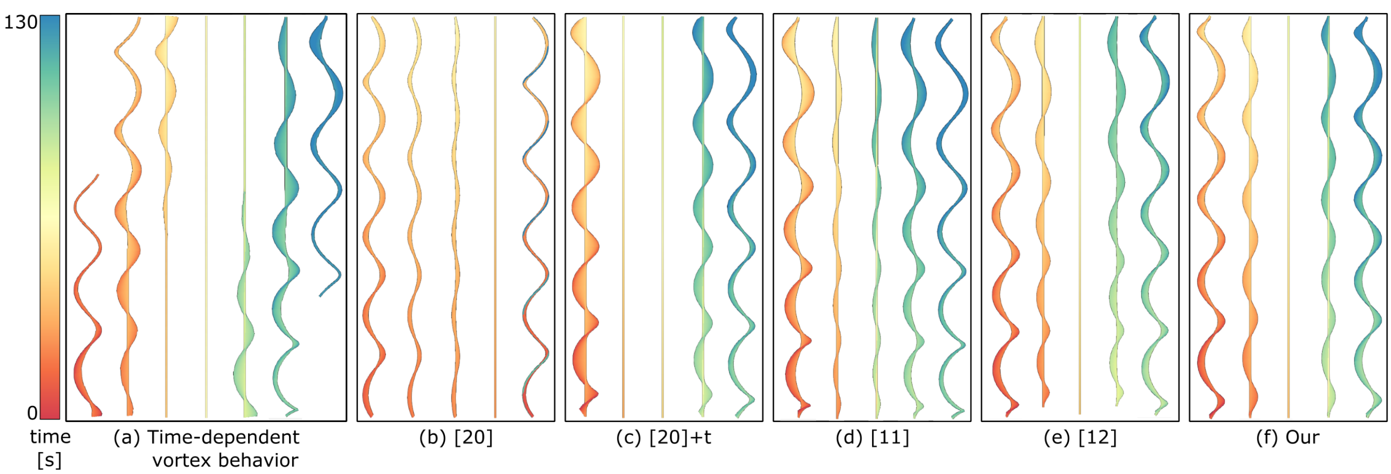

Fig. 14. Clustering results for an artificially generated instable vortex that occurs, decays and reoccurs over time. We compared our method to MCPD [20], MCPD [20] with time integration, the approach by Liu et al. [11] and Meuschke et al. [12]. Due to the time-dependent vortex behavior, five clusters are expected showing the vortex occurring and reoccurring, the transition between vortex and laminar flow and the laminar flow itself.

cluster instable patterns. These comparisons show that existing similarity measures are less reliable than our new approach.

8.2. Robustness Experiments

To evaluate the robustness of our similarity measure, we added different amounts of noise to the artificially generated vortex of Figure 14a. Figure 15 shows the clustering results of our measure for three noise levels. The different levels were generated by adding a random number *rn* to the 3D spatial components (x,y,z) of a path line point, where *rn* was selected in the of range of $[0,i]$ with $i \in [0.2, 0.6, 1.0]$. Adding noise to the spatial position simulates possible occurring artifacts in measured or simulated data, whereas temporal noise would not occur in measured or simulated data sets due to the predefined time between two successive time steps. Our method is able to detect the five expected clusters of the vortex representing its different stages for the different amounts of noise, which shows that our similarity measure is robust against noise.

Besides the robustness analysis of our similarity measure, we perform a qualitative comparison between AHC with average link and SC as described in Oeltze et al. [13] for the artificially generated vortex and the aneurysm data set DS5. For the artificial vortex, there was no visual difference between the results of both clustering methods. SC leads to the same clusters as depicted in Figure 14f. Figure 16 shows exemplary cluster results for DS5 based on AHC and SC. We yielded quite similar results for both methods, which is similar to the findings by the works of [13, 12], who state that both methods lead to reasonable results for blood flow clustering. An in-depth comparison of these techniques based on our similarity measure would be out of the scope of this paper and part of future work.

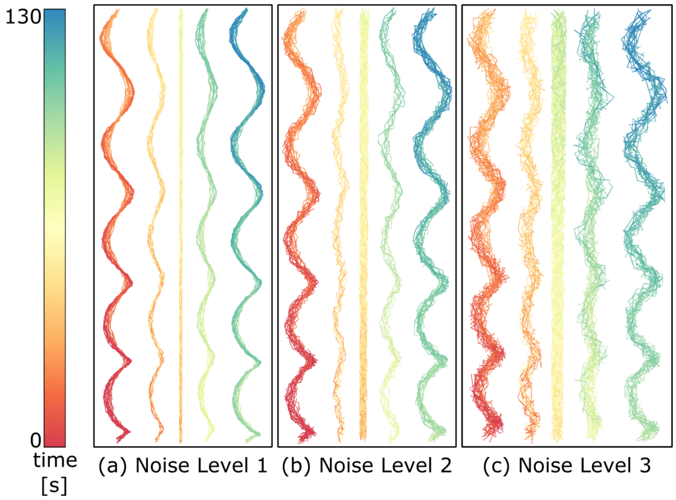

Fig. 15. Clustering results for the artificial vortex of Figure 14a). We added different levels of noise to evaluate the robustness of our similarity measure. Our method is able to detect the expected clusters.

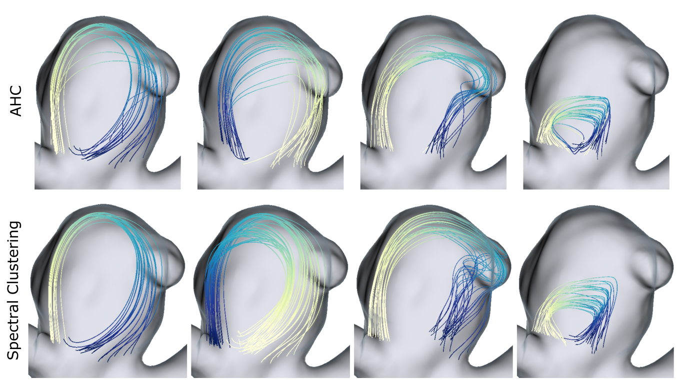

Fig. 16. Exemplary clustering results for DS5 using AHC and SC based on our similarity measure. Both methods lead to qualitatively similar clusters.

8.3. Participants' Cluster Comparison

Due to the absence of a clustering ground truth, this evaluation should show if the participants' sense of path line similarity is coherent with our similarity measure. For this, the participants ranked different path line pairs manually according to similarity for ten cases based on five datasets. Each case contains four pairs, where one path line was the same for all pairs that serves as reference. The cases were generated in the following way: a path line was randomly chosen. Then, the other path lines were ordered according to their similarity. Then, the path lines were categorized in four intervals with approximately the same interval length (based on the similarity measure). For each interval a path line was randomly chosen.

This evaluation was conducted with 12 participants with background in flow visualization ranging from one to six years of experience (four years on average). All pairs of a case were shown side-by-side within the 3D aneurysm surface. If the user rotates one scene, all pairs were rotated synchronously. The participants were asked to order the path lines according to their similarity to the reference line from the highest to the lowest value. Therefore, we color-code the time component on the path lines. Besides the manual ranking, we also ranked the path

Table 1. The results of the manual path line comparisons. The columns correspond to the different cases. One point was given for no mistake (✓), half a point was given for one mistake (❍) and zero points were given for more than one mistake (✗). The last column shows the total number of reached points for each participant.

1	2	3	4	5	6	7	8	9	10	Total
✓	✓	✓	✓	✓	❍	❍	✓	✓	✓	9.0
✓	❍	✓	✓	✓	❍	✓	✓	✓	✓	9.0
✓	✓	✓	✓	✓	✓	❍	✓	✓	✓	9.5
❍	❍	✓	❍	✓	❍	✓	✓	✓	❍	7.5
✓	✓	✓	✓	✓	✓	✓	✓	✓	❍	9.5
✓	❍	✓	❍	✓	✓	✓	✓	✓	❍	8.5
✓	✓	✓	✓	✓	✓	✓	❍	❍	✓	9.0
✓	✗	✓	✓	✓	✓	✓	✓	✓	❍	8.5
✓	❍	✓	✓	✓	❍	✓	❍	✓	❍	8.0
✓	✓	❍	❍	✓	❍	✓	❍	❍	✓	7.5
✓	❍	✓	✓	✓	❍	✗	✓	✓	✓	8.0
❍	❍	✓	✓	✓	✗	✓	✓	✓	✓	8.0

line pairs according to their calculated similarity using our measure. Finally, we compared our rankings with the manual user rankings, see Table 1. For this purpose, we evaluated the order of the path lines with points. If the order of our measure to the participants' order was the same, we gave one point (✓). In case the ordering of one pair was wrong, only half a point (❍) was given. In case two or more orderings were wrong, zero points (✗) were given. The last column of Table 1 shows the total number of points for each participant. A maximum number of ten points could be achieved in total. The higher the value the greater the consistency between our similarity measure and the manual rankings. On average, 8.5 points were reached.

8.4. Informal Expert Feedback

The informal evaluation was conducted with four domain experts, two CFD experts P1, P2 with three and six years of experience, respectively, one neuroradiologist P3 with 15 years of experience and one expert for medical flow visualization P4 with five years of experience, respectively. The informal study was conducted in two steps:

1. Introduction to the framework with the 3D and 2D visualizations of the flow patterns and the interaction techniques.

2. A questionnaire that inquires the importance of intra-aneurysmal flow analysis and the visualization of the clustering results.

The first step is necessary for the experts to familiarize themselves with the tool. Then, the experts answered the questionnaire using a five-point Likert scale ($--$, $-$, $\circ$, $+$, $++$). For the analysis of the Likert scores, we provide the number $S(\cdot)$ of experts who chose the individual scale.

Evaluation of intracranial aneurysm. All domain experts confirmed the importance to analyze quantitative and qualitative flow properties, respectively for the patient-specific rupture risk assessment ($S(++) = 3$; $S(+) = 1$). The simultaneous investigation of these factors was rated as highly important ($S(++) = 4$). The CFD experts stated that a combined analysis

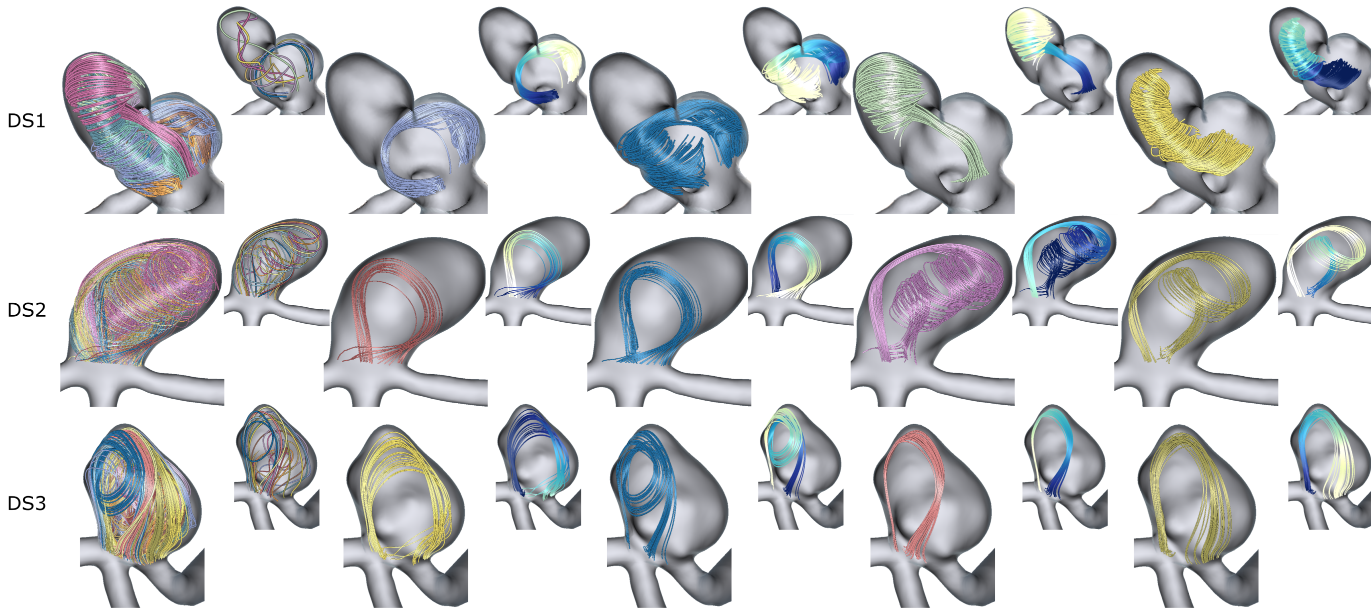

Fig. 17. Exemplary clustering results for three datasets (DS1, DS2, DS3). In the first column, the path lines are color-coded according to their cluster correspondence. As a preview, the cluster representatives are shown. Column 2-5 show different clusters of the dataset, where the path lines in the preview are color-coded according to their temporal component.

is necessary to understand the interplay between specific flow patterns and scalar data such as WSS. Furthermore, we asked about the importance to investigate the distance of flow patterns to the vessel wall that was rated with $S(++) = 4$. P1 stated "[...] vortical flow patterns coming close to the wall are more associated with rupture than more distant patterns." Moreover, they emphasized the importance of the data exploration during the whole cardiac cycle, because it is unknown if the aneurysm rupture risk is higher at the systole or diastole ($S(++) = 4$).

Flow Pattern Recognition. The experts evaluated visualization techniques to recognize flow patterns. One possibility is to show all path lines simultaneously in an animated way. This was considered as inappropriate due to occlusion problems and visual clutter ($S(-) = 1$; $S(--) = 3$). Coloring the path lines due to their cluster affiliation slightly improves the identification of flow patterns ($S(\circ) = 1$; $S(-) = 3$). In contrast, the selection of individual clusters based on the 3D view per mouse click was assessed as very appropriate ($S(+) = 1$; $S(++) = 3$).

3D Cluster Visualization. All experts confirmed that the 3D visualization of the cluster representatives allows a reasonable simplification of the complex flow behavior ($S(++) = 4$). The CFD experts stated the cluster representatives support the assessment of the most prominent flow patterns, which is one their main tasks, see Section 5. Moreover, they stated that the surface transparency reveals the qualitative flow behavior ($S(++) = 4$).

2D Cluster Visualization. All participants found that the map provides a fast overview about a selected scalar field ($S(++) = 3$; $S(+) = 1$). Moreover, they confirmed that the path line projection on the map allows a fast detection of possible rupture-prone wall regions ($S(++) = 2$; $S(+) = 2$). In addition, the experts stated that the 2D map reduces the exploration effort in 3D ($S(++) = 3$; $S(+) = 1$). However, for the assessment of the most prominent flow patterns, P1, P2 preferred the 3D cluster representatives. P3 stated the map would support the comparison of ruptured and non-ruptured cases due to simplified visualization of scalar and vectorial data. The suitability of the plane-based visualization to support the detection of the flow behavior was rated more controversially with $S(+) = 2$ and $S(\circ) = 2$. P2 and P3 argued that the 2D map in combination with the 3D view is sufficient to understand individual flow patterns. Moreover, the experts wished to visualize the used plane also in the 3D view to better understand the underlying projection. Furthermore, we asked if the color-coding of the ostium in the 3D and 2D view provides a visual correspondence between both views, which was confirmed ($S(++) = 4$). In addition, the selection of individual points on the map, followed by changing the camera in 3D, was described as helpful ($S(++) = 2$; $S(+) = 2$).

Finally, we qualitatively evaluated our clustering results with the experts. They visually inspected clusters and stated that they should be spatially compact and temporally coherent. Figure 17 shows exemplary results for three datasets DS1, DS2 and DS3. In the first column, the path lines are color-coded according to their cluster correspondence and the cluster representatives are shown as a preview. Moreover, four clusters per dataset are depicted, where the temporal component is color-coded. All clusters are spatio-temporally compact. For example, the purple and blue cluster of DS1 are spatially very similar, but exhibit an opposite temporal behavior. Thus, they are not grouped together. Reoccurring patterns over time are grouped into different clusters such as the pink and yellow cluster of DS2.

8.5. Performance

Computation times of our approach are listed in Table 2. Memory consumption is not critical. We measured the computation time of the similarity matrix and the clustering, which dependents on the number of path lines and their average number of vertices (columns 2-3 in Table 2). Moreover, we determine the computation time of the map, which depends on the number of mesh triangles (column 6 in Table 2). The timings were taken on an Intel Core i7 CPU with 2 GHz, 12 GB RAM and an NVidia GeForce GT540M. The computation of the similarity matrix represents the bottleneck, where the clustering is quite fast. The computation of the map varies between 1.1 and 6.8 s, which has to be calculated just once. For the visualization, we reach real-time frame rates of 60 frames per second.

Table 2. Timings $[s]$ of path line clustering and 2D map computation.

Dataset	#Path lines	#Vertices (∅)	Similarity Matrix $[s]$	AHC $[s]$	#Mesh Triangles	2D Map $[s]$
DS1	3218	138	2671	26.9	57.912	6.8
DS2	1932	209	1878	12.3	27.534	3.0
DS3	7999	117	5584	53.4	63.132	4.4
DS4	1704	146	1563	9.2	20.974	1.1
DS5	1435	128	1213	7.1	55.192	6.2

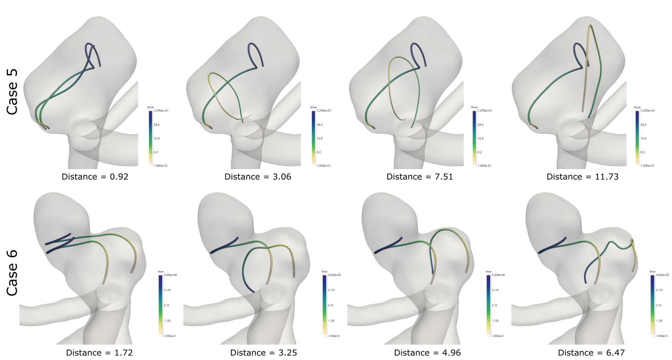

Fig. 18. Exemplary cases from the manually performed path line comparisons with the calculated distances by our method below. The most similar (left) and the most dissimilar pair (right) were correctly ranked by all participants. Deviations occurred for the middle pairs.

9. Discussion

Similarity Validation. Due to the absence of a ground truth to validate our clustering results, we evaluate if our similarity measure leads to plausible results. For this purpose, we compared our calculated similarities with manually prepared similarity rankings of our participants. The experts stated that path lines are similar, if they have a low spatial distance and occur in similar time intervals. In contrast, path lines that occur in different spatial areas or time intervals are classified as less similar. Moreover, path lines that are neither spatially nor temporally similar should get very low similarity values. Our results were consistent with the manual orders in 8.5 points on average. Thus, in most cases, the calculated similarity values conforms to the rankings of the participants. The expert's rankings of cases, showing stronger differentiations in their spatial and temporal behavior, i.e. case 5, conform to our calculated ranking, see Figure 18. Deviations occurred for cases with a more complex flow behavior, such as Case 6, see Figure 18. They ranked the most similar and the most dissimilar pair correctly for almost all cases, but interchanged the second and third rank. The reason therefore were problems to visually estimate the distances between corresponding points based on the temporal component. The participants stated that they are less confident with their estimations for these cases and thus, they would prefer to use our measure. In addition, generating such a ground truth is challenging. Path lines would have to be labeled manually according to predefined types. This would be a time-consuming and subjective process, which is highly affected by visual clutter. The time-dependent behavior of the data would further complicates this process.

In contrast to existing clusterings, our method allows an analysis of flow patterns that are not stable over the cardiac cycle, since instability is (besides complexity) a major predictor for rupture risk [6]. Vortices that only occur during a specific time interval may be investigated with our approach. Such patterns would probably be missed with a static clustering depending on the selected time step for seeding.

Robustness. We could show that our method is robust against noise. However, the measure depends on the most dissimilar path line to ensure that $D(case\,1) \leq D(case\,3)$. Thus, our measure might count the same pair of path lines either as relatively similar, or as more dissimilar, depending on the presence of outliers. In our cases, this does not lead to inappropriate results. To overcome this limitation, we would have to change the calculation of $(D)_{ij}$ to $(D)_{ij} = 1 - \frac{1}{(\overline{D}_{ij}+1)} + J_{ij}$ or $(D)_{ij} = 1 - \exp(-(\frac{\overline{D}_{ij}^2}{\sigma})) + J_{ij}$, where σ is a user-defined variable. However, with these new calculations of $(D)_{ij}$, the distance values would not change linearly. This also might lead to inappropriate clustering results.

Aneurysm Shape. Currently, the map is designed for saccular shaped aneurysms, where one ostium can be defined. Fusiform aneurysms are dilatations over a certain length of the vessel, where two regions separate the aneurysm from the parent vessel. To handle their cylindrical shape, we would have to adapt the 2D mapping by defining three cutting edges, two along the ostium contours and one connecting these two cutting edges. Then, we would unfold the cylindrical structure using the LSCM parametrization. However, saccular aneurysms occur significantly more frequently ($\approx 90\%$ of all treated aneurysms). In addition, CFD does not consider the mechanical wall deformation due to static segmentation of the aneurysm surface. However, intracranial vessels exhibit a low deformation due to the cardiac pulsation. Therefore, a static segmentation allows an estimation of the distance of flow patterns to the wall.

Uncertainty. The individual preprocessing steps, image reconstruction, segmentation, and choice of inflow boundary condition are related to uncertainties [43, 44, 45]. To reconstruct angiography images as input for the surface extraction, different reconstruction kernels can be used. Depending on the selected kernel, the vessel diameter and ostium area is influenced, which further leads to differences in hemodynamic values such as pressure and flow magnitude. In addition, the shape of the reconstructed surface and CFD results depend on the selected segmentation method. Finally, the chosen boundary conditions for the CFD simulation influence the resultant vector fields. Deriving flow rates from known patient-specific flow rates could lead to uncertainties in the CFD results, since flow rates depend on different factors such as sex, body size and normal or pathological variants of vascular anatomy. However, patient-specific flow rates are rarely available. In summary, uncertainties arising from the individual preprocessing steps could lead to inaccuracies in the resultant flow patterns, i.e., flow patterns could be traced that are actually not existing. However, until now there is no clear recommendation which methods should be used for preprocessing. A more detailed analysis of possibly arising uncertainties is beyond the scope of this work.

Findings. During the evaluation it was transpired that the 3D and 2D depictions represent a useful combination for an efficient exploration of flow patterns. The experts liked the concept of the linked and juxtaposed 3D and 2D depictions, which avoids switching between the views. The 3D view allows a detailed analysis of individual flow patterns. Thus, our experts were able to find correlations between rupture-relevant flow patterns and high-risk wall regions, see Figure 19. Here, for two datasets DS_1 and DS_2 the WSS is color-coded and the pressure is depicted by hatching. The experts analyzed individual clusters of both cases. In DS_1 they detected a flow pattern that orthogonally hits the wall during the whole cardiac cycle and could lead to rupture. Conversely, the flow patterns of DS_2 run along the wall and have therefore been assessed as less rupture-prone despite the increased pressure and WSS values. However, in some cases the experts were unsure if the current flow pattern is closer to the anterior or posterior wall of the vessel. Therefore, they wished to have additional clipping planes or a 2D color map, coding the distance to the respective wall side.

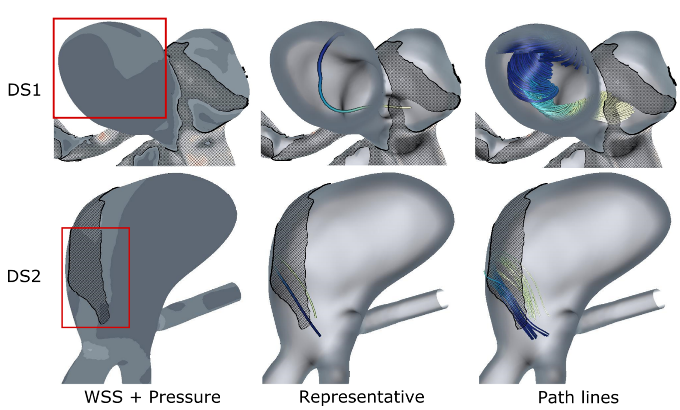

Fig. 19. Detailed flow pattern exploration by using different cluster visualizations for two datasets DS_1 and DS_2. WSS is color-coded and pressure is depicted by hatching. DS_1 can be assumed to be more rupture-prone due to the flow pattern that orthogonally hits the wall. DS_2 was assessed as less rupture-prone due to flow patterns going along the wall despite the increased pressure and WSS values.

The 2D map gives a fast overview about possible correlations between flow patterns and scalar wall properties. By depicting the path lines as circles with depth-dependent halos, the color-coded scalar field can be analyzed simultaneously. Existing approaches used cut away techniques [30] or surface transparency for this purpose [24]. However, with these methods, the visibility of the displayed scalar field on the surface is severely restricted, which is avoided with our map-based visualization.

Due to the different assessment of the plane-based cluster depiction, we provide an optional activation of this view. Moreover, the experts wished to have more interaction techniques on the map that support the identification of the corresponding path lines in 3D. This could be realized by selecting a specific circle region on the map, followed by highlighting the corresponding path lines in 3D. In addition, the map-based path line rendering using circles was emphasized positively by all experts, because it provides a useful simplification of the complex 3D flow.

Further Applications. Our path line clustering may also be helpful to explore the predicted blood flow after different treatment options, such as coiling and stenting. Therefore, a visualization of the used stent or coils would be required. Moreover, a comparative visualization of flow patterns before and after treatment would be necessary to assess the applicability of the used treatment option. Other important applications are research and student education. CFD also plays an essential role in other vascular structures, such as the aorta, to better understand CVDs, e.g., aortic aneurysms. Our method would probably be useful in these applications as well. However, in the aorta, fusiform aneurysms occur more frequently. Therefore, we should extend our mapping to fusiform aneurysms.

10. Conclusion and Future Work

We presented a method for clustering path lines in cerebral aneurysms. Besides the aneurysm separation, our method performs fully automatically. Our similarity measure extends the MCPD, a reliable measure to determine streamline similarities. We achieved convincing results compared to manual similarity estimations of path lines. For clustering, we used AHC, an established method to group integral lines. This assures a comparability of datasets and reproducibility of the results. In contrast, a manual analysis of flow patterns is time-consuming. A common advantage of AHC is the possibility to incorporate expert knowledge. The cluster number can be changed, which allows an investigation of alternative cluster configurations.

At the moment, there is no calculable value that indicates the rupture probability, because rupture seems to depend on various factors, i.e., on inflammation processes that cannot be modeled until now. Moreover, clinicians evaluate the rupture risk differently based on their experience. Our tool provides a faster and more objective analysis of suspicious flow patterns into clinical discussions by providing a time-dependent clustering and efficient exploration techniques. Our domain experts stated that they want to use our framework for a larger study in the future to investigate possible correlations between flow patterns and rupture and to analyze flow patterns with different stents.

In the future, we want to perform a comparison of our current similarity measure and the suggested solution in Section 9 to overcome the global distance calculation. Furthermore, the generation of the 2D map is currently restricted to the aneurysm. We would like to compare other mappings that preserve the aneurysm shape including adjacent vessels. This would be important for the analysis of different stents and their influence on the blood flow in adjacent vessels. In addition, our technique will form the basis for an automatic classification of flow patterns based on the manual approach by Cebral et al. [6]. Related to this, we want to integrate an automatic determination of inflow jets and impingement zones. Another interesting point would be a perception-based user study that evaluates concepts, i.e., color or illustrative techniques, to encode scalar values on lines such as the distance of path lines to the aneurysm wall.

11. Appendix

Mean distance of two path lines: The mean distance of both path lines in the time interval $[t_i, t_{i+1}]$ is determined by:

$$\begin{aligned}
\overline{D}^{kl}(t_i,t_{i+1}) &= \lim_{N\to\infty}\sum_{i=0}^{N}\frac{1}{N+1}\underbrace{\|c_k(i/N)-c_l(i/N)\|}_{d(i/N)} \\
&= \lim_{N\to\infty}\sum_{i=0}^{N}\left(\underbrace{\frac{i+1}{N+1}}_{t_{i+1}}-\frac{i}{N+1}\right)\cdot d(i/N) \\
&= \lim_{N\to\infty}\sum_{i=0}^{N}(t_{i+1}-t_i)\cdot d(t_i) \\
&= \int_0^1 d(t)\,\mathrm{d}t.
\end{aligned}$$

Thus, the mean distance of two moving particles is determined by a novel approach using the integral of the distances.

Integral form: The integral of the mean distance of two curves given in Eq. 2 is of the form:

$$\overline{D}^{kl}(t_i,t_{i+1}) = \int_0^1 d(t)\,\mathrm{d}t = \int_0^1 \sqrt{a+2bt+ct^2}\,\mathrm{d}t, \qquad (7)$$

where $a = \langle \mathbf{p}_i^k - \mathbf{p}_i^l, \mathbf{p}_i^k - \mathbf{p}_i^l\rangle$, $b = \langle \mathbf{p}_i^k - \mathbf{p}_i^l, \mathbf{p} - \mathbf{p}_i^k - \mathbf{p}_{i+1}^l + \mathbf{p}_i^l\rangle$, and $c = \langle \mathbf{p}_{i+1}^k - \mathbf{p}_i^k - \mathbf{p}_{i+1}^l + \mathbf{p}_i^l, \mathbf{p} - \mathbf{p}_i^k - \mathbf{p}_{i+1}^l + \mathbf{p}_i^l\rangle$. This integral can be solved analytically.

Acknowledgments

This work was partially funded by the BMBF (STIMULATE:13GW0095A). The authors like to thank Philipp Berg for the fruitful discussions on these and related topics.

References

[1] Xiang, J, Natarajan, SK, Tremmel, M, Ma, D, Mocco, J, et al., . Hemodynamic–morphologic discriminants for intracranial aneurysm rupture. Stroke 2011;42(1):144–52.

[2] Nieuwkamp, DJ, Setz, LE, Algra, A, Linn, FH, de Rooij, NK, Rinkel, GJ. Changes in case fatality of aneurysmal subarachnoid haemorrhage over time, according to age, sex, and region: a meta-analysis. The Lancet Neurology 2009;8(7):635–42.

[3] Wermer, MJ, van der Schaaf, IC, Algra, A, Rinkel, GJ. Risk of rupture of unruptured intracranial aneurysms in relation to patient and aneurysm characteristics. Stroke 2007;38(4):1404–10.

[4] Cebral, JR, Mut, F, Weir, J, Putman, CM. Association of hemodynamic characteristics and cerebral aneurysm rupture. Am J Neuroradiol 2011;32(2):264–70.

[5] Appanaboyina, S, Mut, F, Löhner, R, Putman, C, Cebral, J. Simulation of intracranial aneurysm stenting: Techniques and challenges. Computer Methods in Applied Mechanics and Engineering 2009;198(45):3567–82.

[6] Cebral, JR, Castro, MA, Burgess, JE, Pergolizzi, RS, Sheridan, MJ, Putman, CM. Characterization of cerebral aneurysms for assessing risk of rupture by using patient-specific computational hemodynamics models. Am J Neuroradiol 2005;26(10):2550–59.

[7] Born, S, Pfeifle, M, Markl, M, Gutberlet, M, Scheuermann, G. Visual Analysis of Cardiac 4D MRI Blood Flow Using Line Predicates. IEEE Trans Vis Comput Graph 2013;19:900–12.

[8] Gasteiger, R, Lehmann, DJ, van Pelt, R, Janiga, G, Beuing, O, Vilanova, A, et al. Automatic Detection and Visualization of Qualitative Hemodynamic Characteristics in Cerebral Aneurysms. IEEE Trans Vis Comput Graph 2012;18(12)(12):2178–87.

[9] Köhler, B, Gasteiger, R, Preim, U, Theisel, H, Gutberlet, M, Preim, B. Semi-automatic Vortex Extraction in 4D PC-MRI Cardiac Blood Flow Data using Line Predicates. IEEE Trans Vis Comput Graph 2013;19(12):2773–82.

[10] Englund, R, Ropinski, T, Hotz, I. Coherence Maps for Blood Flow Exploration. In: EG VCBM. 2016, p. 79–88.

[11] Liu, R, Guo, H, Zhang, J, Yuan, X. Comparative visualization of vector field ensembles based on longest common subsequence. In: IEEE PacificVis. 2016, p. 96–103.

[12] Meuschke, M, Lawonn, K, Köhler, B, Preim, U, Preim, B. Clustering of Aortic Vortex Flow in Cardiac 4D PC-MRI Data. In: Bildverarbeitung für die Medizin. 2016, p. 182–7.

[13] Oeltze, S, Lehmann, DJ, Kuhn, A, Janiga, G, Theisel, H, Preim, B. Blood Flow Clustering and Applications in Virtual Stenting of Intracranial Aneurysms. IEEE Trans Vis Comput Graph 2014;20(5):686–701.

[14] McLoughlin, T, Jones, MW, Laramee, RS, Malki, R, Masters, I, Hansen, CD. Similarity measures for enhancing interactive streamline seeding. IEEE Trans Vis Comput Graph 2013;19(8):1342–53.

[15] van Pelt, R, Jacobs, S, ter Haar Romeny, B, Vilanova, A. Visualization of 4D Blood-Flow Fields by Spatiotemporal Hierarchical Clustering. Comput Graph Forum 2012;31(3pt2):1065–74.

[16] Gambaruto, A, João, A. Flow Structures in Cerebral Aneurysms. Comput Fluids 2012;65:56–65.

[17] Neugebauer, M, Lawonn, K, Beuing, O, Berg, P, Janiga, G, Preim, B. AmniVis - A System for Qualitative Exploration of Near-Wall Hemodynamics in Cerebral Aneurysms. Comput Graph Forum 2013;32(3):251–60.

[18] Salzbrunn, T, Scheuermann, G. Streamline Predicates. IEEE Trans Vis Comput Graph 2006;12(6):1601–12.

[19] van Pelt, R, Gasteiger, R, Lawonn, K, Meuschke, M, Preim, B. Comparative Blood Flow Visualization for Cerebral Aneurysm Treatment Assessment. Comput Graph Forum 2014;33(3)(3):131–40.

[20] Corouge, I, Gouttard, S, Gerig, G. Towards a shape model of white matter fiber bundles using diffusion tensor MRI. In: IEEE International Symposium on Biomedical Imaging. 2004, p. 344–47.

[21] Hastreiter, P, Rezk-Salama, C, Tomandl, B, Eberhardt, KEW, Ertl, T. Fast analysis of intracranial aneurysms based on interactive direct volume rendering and CTA. In: Proc. of MICCAI. 1998, p. 660–69.

[22] Tomandl, B, Hastreiter, P, Iserhardt-Bauer, S, Köstner, NC, et al., . Standardized evaluation of CT angiography with remote generation of 3D video sequences for the detection of intracranial aneurysms. Radiographics 2003;23(2):e12.

[23] Goubergrits, L, Schaller, J, Kertzscher, U, van den Bruck, N, Poethkow, K, Petz, C, et al. Statistical Wall Shear Stress Maps of Ruptured and Unruptured Middle Cerebral Artery Aneurysms. J R Soc Interface 2012;9(69):677–88.

[24] Meuschke, M, Voß, S, Beuing, O, Preim, B, Lawonn, K. Combined Visualization of Vessel Deformation and Hemodynamics in Cerebral Aneurysms. IEEE Trans Vis Comput Graph 2017;23(1):761–70.

[25] Lévy, B, Petitjean, S, Ray, N, Maillot, J. Least Squares Conformal Maps for Automatic Texture Atlas Generation. ACM Trans Graph 2002;21(3):362–71.

[26] Tao, J, Huang, X, Qiu, F, Wang, C, Jiang, J, Shene, CK, et al. VesselMap: A web interface to explore multivariate vascular data. Computers & Graphics 2016;.

[27] Gasteiger, R, Neugebauer, M, Beuing, O, Preim, B. The FLOWLENS: A Focus-and-Context Visualization Approach for Exploration of Blood Flow in Cerebral Aneurysms. IEEE Trans Vis Comput

Graph 2011;17(12):2183–92.
[28] Lawonn, K, Gasteiger, R, Preim, B. Adaptive Surface Visualization of Vessels with Animated Blood Flow. Comput Graph Forum 2014;33(8):16–27.
[29] Gambaruto, A, João, A. Flow Structures in Cerebral Aneurysms. Comput Fluids 2012;65:56–65.
[30] Lawonn, K, Glaßer, S, Vilanova, A, Preim, B, Isenberg, T. Occlusion-free Blood Flow Animation with Wall Thickness Visualization. IEEE Trans Vis Comput Graph 2015;22(1):728–37.
[31] Lall, R, Eddleman, C, Bendok, B, Batjer, H. Unruptured Intracranial Aneurysms and the Assessment of Rupture Risk based on Anatomical and Morphological Factors: Sifting through the Sands of Data. Neurosurg Focus 2009;26(5):E2.
[32] Janiga, G, Berg, P, Sugiyama, S, Kono, K, Steinman, DA. The Computational Fluid Dynamics Rupture Challenge 2013—Phase I: prediction of rupture status in intracranial aneurysms. Am J Neuroradiol 2015;36(3):530–36.
[33] Futami, K, Nambu, I, Kitabayashi, T, Sano, H, et al., . Inflow hemodynamics evaluated by using four-dimensional flow magnetic resonance imaging and the size ratio of unruptured cerebral aneurysms. Neuroradiology 2017;:1–8.
[34] Marcelo Castro and Christopher Putman and Alessandro Radaelli and Alejandro Frangi and Juan Cebral, . Hemodynamics and Rupture of Terminal Cerebral Aneurysms. Academic Radiology 2009;16(10):1201–07.
[35] Nakayama, T, Sugiyama, Si, Ohta, M. Classification of Blood Flow in Cerebral Aneurysm Considering the Parent Artery Curves. In: Int Mech Eng Congress Expo. 2013, p. V03AT03A033–V03AT03A033.
[36] Mönch, T, Neugebauer, M, Preim, B. Optimization of Vascular Surface Models for Computational Fluid Dynamics and Rapid Prototyping. In: Workshop on Digital Engineering. 2011, p. 16–23.
[37] Schöberl, J. An Advancing Front 2D/3D- Mesh Generator Based On Abstract Rules. Comput Vis Sci 1997;1:41–52.
[38] Berg, P, Roloff, C, Beuing, O, Voss, S, et al., . The Computational Fluid Dynamics Rupture Challenge 2013–Phase II: Variability of Hemodynamic Simulations in Two Intracranial Aneurysms. J Biomech Eng 2015;137(12):121008.
[39] Salvador, S, Chan, P. Determining the number of clusters/segments in hierarchical clustering/segmentation algorithms. In: IEEE International Conference on Tools with Artificial Intelligence. 2004, p. 576–84.
[40] Gasteiger, R, Neugebauer, M, Kubisch, C, Preim, B. Adapted Surface Visualization of Cerebral Aneurysms with Embedded Blood Flow Information. In: EG VCBM. 2010, p. 25–32.
[41] O'Donnell, LJ, Westin, CF, Golby, AJ. Tract-based morphometry for white matter group analysis. Neuroimage 2009;45(3):832–44.
[42] Everts, MH, Bekker, H, Roerdink, JB, Isenberg, T. Depth-dependent halos: Illustrative rendering of dense line data. IEEE Trans Vis Comput Graph 2009;15(6).
[43] Berg, P, Saalfeld, S, Voss, S, Redel, T, Preim, B, Janiga, G, et al. Does the DSA reconstruction kernel affect hemodynamic predictions in intracranial aneurysms? An analysis of geometry and blood flow variations. J Neurointerv Surg 2017;:neurintsurg–2017–012996.
[44] Sen, Y, Qian, Y, Avolio, A, Morgan, M. Image segmentation methods for intracranial aneurysm haemodynamic research. Journal of Biomechanics 2014;47(5):1014–1019.
[45] Valen-Sendstad, K, Piccinelli, M, KrishnankuttyRema, R, Steinman, DA. Estimation of inlet flow rates for image-based aneurysm CFD models: where and how to begin? Ann Biomed Eng 2015;43(6):1422–31.